High-Resolution 4D Preclinical Single-Photon Emission Computed Tomography/X-ray Computed Tomography Imaging of Technetium Transport within a Heterogeneous Porous Media

Dogan, Mine; Moysey, Stephen M.J.; Ramakers, Ruud M.; Devol, Timothy A.; Beekman, Frederik J.; Groen, Harald C.; Powell, Brian A.

DOI
10.1021/acs.est.6b04172

Publication date
2017

Document Version
Final published version

Published in
Environmental Science & Technology (Washington)

Environmental Science & Technology

Article

pubs.acs.org/est

High-Resolution 4D Preclinical Single-Photon Emission Computed Tomography/X-ray Computed Tomography Imaging of Technetium Transport within a Heterogeneous Porous Media

Mine Dogan,*[,†] Stephen M. J. Moysey,[†] Ruud M. Ramakers,[‡,§] Timothy A. DeVol,[†] Frederik J. Beekman,[‡,§] Harald C. Groen,[‡] and Brian A. Powell[†]

[†]Environmental Engineering and Earth Sciences, Clemson University, Clemson, South Carolina 29634, United States

[‡]MILabs, 3584 CX Utrecht, The Netherlands

[§]Section Radiation, Detection & Medical Imaging, TU-Delft, 2628 CD Delft, The Netherlands

Supporting Information

ABSTRACT: A dynamic ^{99m}Tc tracer experiment was performed to investigate the capabilities of combined preclinical single photon emission computed tomography (SPECT) and X-ray computed tomography (CT) for investigating transport in a heterogeneous porous medium. The experiment was conducted by continuously injecting a ^{99m}Tc solution into a column packed with eight layers (i.e., soil, silica gel, and 0.2−4 mm glass beads). Within the imaging results it was possible to correlate observed features with objects as small as 2 mm for the SPECT and 0.2 mm for the CT. Time-lapse SPECT imaging results illustrated both local and global nonuniform transport phenomena and the high-resolution CT data were found to be useful for interpreting the cause of variations in the ^{99m}Tc concentration associated with structural features within the materials, such as macropores. The results of this study demonstrate SPECT/CT as a novel tool for 4D (i.e., transient three-dimensional) noninvasive imaging of fate and transport processes in porous media. Despite its small scale, an experiment with such high resolution data allows us to better understand the pore scale transport which can then be used to inform larger scale studies.

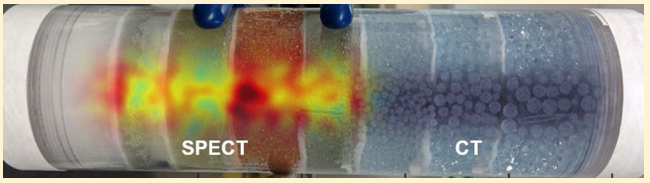

INTRODUCTION

On the basis of traditional flow-through column experiments alone, it is difficult to untangle how the reactive transport of solutes is influenced by biogeochemical processes (e.g., sorption and redox reactions) and flow complexities (e.g., preferential flow and mass transfer to immobile zones) caused by soil physical heterogeneity (i.e., grain size/sorting, macropores). Biologic elements, such as plant roots and microbial communities, further complicate the coupling between flow and biogeochemical systems. In the past, modeling studies and after the fact destructive sampling were relied on as primary tools to provide direct illustrations of how physical, chemical, and biological processes control detailed spatial and temporal distributions of water and chemicals within a soil volume. Today medical imaging techniques have the potential to achieve dynamic, high-resolution monitoring of solutes and soil structures that could provide valuable insights to understanding biogeochemical systems and governing processes at a scale that is otherwise difficult to investigate in situ.

Methods such as X-ray computed tomography (i.e., CT scans) and magnetic resonance imaging (MRI) are increasingly providing the opportunity to gain empirical insights into subsurface transport processes by allowing us to nondestructively image the interior of a porous medium in the laboratory.[1−3] In some cases, these imaging modalities have been used to monitor the dynamics of unsaturated flow[4,5] and transport,[6] the distribution of organic contaminants,[7] or the accumulation of biofilms.[8] A limitation of CT and MRI imaging, however, is that these techniques typically provide a qualitative assessment of the physical structure of the soil or fluid distribution and are not well suited to quantifying solute transport. For example, CT relies on the attenuation of X-rays passed through a sample to image density differences that distinguish pore space (e.g., air or water of low density) and grains (e.g., minerals of high density) as well as the materials with densities in between (e.g., plant roots, biofilms), but it does not allow for targeting of specific chemicals.

In contrast, the radioactive decay of some isotopes results in the production of γ rays that can pass through a soil and be measured by detectors located outside of the sample. These isotopes may therefore be used as reactive tracers for direct, noninvasive tracking of solute transport within a heterogeneous and biogeochemically active soil. Hao et al.,[9] for example, performed a column experiment where a sodium iodide scintillation detector was used to monitor the accumulation of ^{22}Na ($t_{1/2}$ = 2.60 yrs, γ-energy = 511 and 1275 keV) on grain surfaces of silica gel in response to increases in the pH of the influent solution to a column. Corkhill et al.[10] provide an

Received: August 17, 2016
Revised: January 26, 2017
Accepted: January 27, 2017
Published: January 27, 2017

DOI: 10.1021/acs.est.6b04172
Environ. Sci. Technol. 2017, 51, 2864−2870

example where a clinical gamma-camera[11] was used to map the 2D distribution of ^{99m}Tc (the metastable form of technetium-99; $t_{1/2}$ = 6.0 h, γ-energy =140 keV) to determine in situ parameters for transport. In contrast, Lear et al.[12] and Vandehey et al.[13] investigated microbially facilitated redox reactions by monitoring how a ^{99m}Tc tracer partitions between the fluid and soils in microcosms. While these studies are outstanding examples of how radioactive materials can be used as tracers, they do not capture the full, three-dimensional complexity of transport in heterogeneous porous media.

Single-photon emission computed tomography (SPECT) and combined SPECT/CT are widely established biomedical imaging modalities used to monitor the physiologic function of specific tissues using molecules labeled with radiotracers administered to patients in clinical settings.[14] With SPECT, multiple planar gamma ray images under different view-angles are captured and used to reconstruct the three-dimensional distribution of the radiotracer within a subject, or in our case a soil sample. Perret et al.[15] and Boutchko et al.[16] give examples where clinical SPECT systems are used to monitor nonuniform ^{99m}Tc transport in inhomogeneous media. Vandehey et al.[17] performed a detailed performance assessment of a clinical SPECT system to verify the resolution, uniformity, and linearity of the images obtained for nonstandard geologic imaging applications. Recently, Pini et al.[18] utilized 3D positron emission tomography (PET) imaging, a method related to SPECT, to monitor ^{11}C transport and combined this information with high resolution CT images to model the transport behavior through a rock sample.

The resolution of clinical SPECT systems within soils (e.g., 7.9 mm in the study of Vandehey et al.[17]) is relatively poor for the detailed investigation of localized transport phenomena. In contrast, high-resolution preclinical SPECT imaging, that is, systems configured for imaging of small animals rather than humans, are available[19] and considered to be able to achieve half-millimeter[20] or even quarter millimeter[21] resolutions depending on the sample size and length of the scans, suggesting that details of radionuclide distributions within a soil, such as in macropores and aggregates, can be achieved.

In this study, we evaluate the use of combined preclinical SPECT and CT scans for 4D imaging transport of ^{99m}Tc in heterogeneous porous media, where 4D refers to three-dimensional time-lapse imaging. To assist in the evaluation of the resolution of the SPECT and CT data, we used a column packed with six layers of glass beads ranging in size from about 200 μm to 4 mm, a layer of silica gel, and one soil layer. We additionally embedded capillary tubes with a 1.1 mm inner diameter within each material. The soil layer comprised soil from the US Department of Energy's Savannah River Site (SRS) to allow for evaluation of the imaging techniques within a natural material (chemical and physical characteristics of the SRS soil are given in Supporting Information, Table 1). The clean up of legacy wastes from weapons production is a major undertaking at the SRS and evaluation of the fate and transport of radioisotopes, such as technetium, is a critical component for the risk analysis of subsurface waste disposition.[22]

Both time-lapse imaging during flow and higher resolution imaging while the flow was stopped were performed to assess differences in the imaging results under each of these conditions. Our goal in this study is assessing the viability of SPECT/CT for monitoring the in situ transport behavior of technetium through porous media. The materials used in this experiment were therefore selected to provide a range of pore geometries, sizes, and mineral surfaces that could be used to investigate the performance of SPECT/CT under typical environmental (rather than biological) sample conditions.

MATERIALS AND METHODS

The transport experiment was conducted using an acrylic column with an inner diameter of 46.5 mm and length of 156.4 mm packed under ambient conditions. Figure 1a shows how the column was packed in layers using eight different materials ordered from fine to coarse (i.e., silica gel, 210−250 μm glass beads, 500 μm glass beads, SRS soil, and 1 mm, 2 mm, 3 mm, and 4 mm glass beads). Silica gel (SiO_2) used in this column is manufactured for column chromatography with a density range of 2.6−2.8 g/cm^3 and specific surface area of 480 to 550 m^2/g (Cat. No: 1.07734.1003, EMD Millipore, Billerica, MA, USA). The 210−250 μm (Cat. No: 18902, Polysciences Inc., Warminster, PA, USA) and 500 μm (Cat. No: 11079105, BioSpec Products, Bartlesville, OK, USA) glass beads are made of soda lime glass with an approximate density of 2.5 g/cm^3 and calculated specific surface area of 96−114 and 48 cm^2/g, respectively. The larger beads (Cat. No's: 03000200, 03000400, 03000600, and 03000800, Propper Mfg. Co. Inc., Long Island City, NY, USA) are fire-hardened glass with an approximate density of 2.2 g/cm^3 and specific surface areas ranging from 6 to 27 cm^2/g. A glass fiber filter (Cat. No: 64798, Metrigard 47 mm diameter, 0.5 μm pore size; Pall Corporation, Port Washington, NY, USA) was placed between each layer while packing to prevent inadvertent mixing of the grains. The SRS soil was a sandy loam (66% sand, 14% silt, 20% clay) obtained from the West Borrow Pit, packed into the column after 24 h of oven drying at 50 °C, and the only geochemically reactive material in the column. The soil has a pH of 4.8 and the clay fraction is >95% kaolinite determined using X-ray diffraction (Siemens D5000 X-ray diffractometer using Cu Kα radiation). Also its surface area is measured as 14.1 m^2/g by N_2 adsorption (Micrometrics ASAP 2000 Surface Area Analyzer). Additionally, three glass capillary tubes (Cat. No: 22-260943, Fisherbrand, Waltham, MA, USA), each approximately 1.5 cm long and with 1.1 mm inner diameter (1.5 mm outer diameter), were placed parallel to the axis of the column within each layer in a triangular pattern. The column was then saturated using distilled and deionized (DDI) water with a pH of approximately 6. The average porosity of the materials was gravimetrically estimated to be about 40% based on initial saturation of the column from dry conditions.

Imaging studies were performed using a VECTor^{4}CT instrument[21] (MILabs, Utrecht, The Netherlands), which is an integrated preclinical SPECT/PET/CT system. The saturated column was inserted horizontally into the imaging instrument, and a high resolution CT scan at 65 kV and 0.29 mA was acquired prior to the initiation of the transport experiment (Figure 1b). SPECT imaging was conducted using three stationary NaI (TI) scintillation detectors and a collimator 98 mm in diameter with 1.5 mm pinholes. The expected resolution with this SPECT system is less than 1 mm and sensitivity is larger than 1500 cps/MBq. The actual resolution achieved depends on the number of γ rays detected during imaging and thus depends on scan time.

The pertechnetate ($^{99m}TcO_4^-$, $t_{1/2}$ = 6 h) working solution was prepared by adding 0.66 mL of normal saline (0.15 mol L^{-1} NaCl) containing 780 MBq $^{99}TcO_4^-$ to 250 mL of DDI water. The pertechnetate ion was selected for this work because of our long-term interest in studying ^{99}Tc transport in the environment. For the oxic conditions of this experiment, the Tc(VII)O_4^- anion is expected to be the dominant form of technetium present in the

DOI: 10.1021/acs.est.6b04172
Environ. Sci. Technol. 2017, 51, 2864−2870

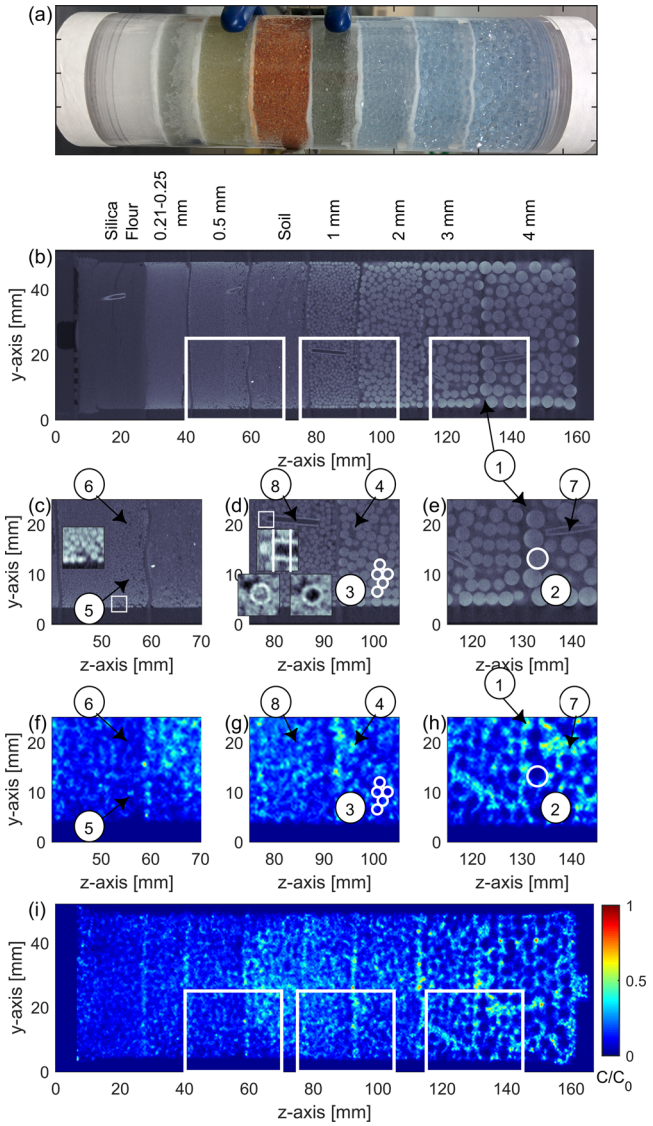

Figure 1. Experimental column was packed with layers containing silica gel, soil, and glass beads between 0.2 and 4 mm as shown in the photograph (a) and a single slice of the reconstructed CT scan located in the center of the column (b). The highest-resolution SPECT reconstruction was obtained by analysis of data collected over a period of 24 h while the flow was stopped (i); the color scale in the SPECT images represents ^{99m}Tc radioactivity levels (normalized to the activity of the working solution at the beginning of the scan) from 0 (blue) to 1 (red). Magnified portions of the CT scan are shown in images c through e with features pointed out as filter paper (1), 4 mm grain (2), 2 mm grains (3), a large pore (4), and capillary tubes embedded within the porous media (7 and 8). Features 5 and 6 correspond to high and low zones of ^{99m}Tc activity, respectively, where no corresponding feature was apparent in the CT scan. The figure insert in image c shows a close-up of 0.5 mm beads in the 3 mm by 3 mm area marked with a white square. The top insert in panel d shows a magnified view of the 3 mm by 3 mm area marked by a white square to illustrate the blockage of the capillary tube by a 1 mm glass bead; the vertical white lines in the inset show the location of perpendicular images across the capillary tube (bottom inserts) to demonstrate the blocked versus open portion of the capillary. Corresponding single slice SPECT images are shown in images f through h, with corresponding features observed in the CT scan identified.

column and will be mobile. Under other experimental conditions (e.g., anoxic pore water) it may, however, be more appropriate to utilize alternative compounds, such as ^{99m}Tc(IV)-DTPA, if conservative transport behavior is desired. The resulting solution contained 3.12 MBq mL^{-1} of $^{99m}TcO_4^-$ at time zero in 0.4 mmol L^{-1} NaCl at pH 6.8 (note this ^{99m}Tc activity concentration corresponds to a molar concentration of 1.64×10^{-10} mol L^{-1}). SPECT images were collected as 180 mL of the working solution was injected into the column at a flow rate of 1.5 mL/min using a Masterflex (Vernon Hills, IL, USA) peristaltic pump. Notably, the pump was intermittently stopped over the course of the experiment to facilitate the collection of the imaging data (specific times are discussed below).

Imaging data were acquired throughout the tracer experiment, both when the pump was turned on and when it was turned off (see Supporting Information, Table 2). While the pump was running, SPECT data were collected continuously to allow for the acquisition of 25 low-resolution, time-lapse reconstructions of the ^{99m}Tc migration; the first four images were collected over 2 min intervals, whereas images later in the experiment were collected over 3 min intervals. These dynamic images were collected to capture the dynamic behavior of the tracer and were acquired in short timeframes to keep the averaging over time at a minimum, therefore their resolution is limited compared to the longer scans. Ten minutes into the injection, however, the pump was stopped to allow for a longer SPECT data acquisition time of 10 min. By stopping the flow we aimed to allow the ^{99m}Tc plume to become stationary, thus avoiding potential temporal blurring caused by active transport during the image acquisition period. After restarting the flow, time-lapse imaging continued, but the flow was subsequently stopped after every 20 min of flow to allow for additional static imaging periods of 10 min. This procedure resulted in the acquisition of six higher resolution images at different times throughout the experiment. Even though the total actual run time for the pump was only 2 h and 3 min, this phase of the experiment took 3 h and 40 min to complete due to the pauses for data collection. Thus, at this point of the experiment approximately two pore volumes of the tracer were passed through the column and more than 50% of the ^{99m}Tc activity for the first half-life was lost as a result of radioactive decay. Subsequently, the flow was stopped and SPECT images were collected over 60 min intervals for 36 h during the decay of the ^{99m}Tc within the column. The first 24 of these images were processed together to create a high resolution SPECT image to investigate the detailed distribution of ^{99m}Tc activity throughout the entire column (Figure 1i).

All SPECT image sets were reconstructed with 0.8 mm voxels (note that under ideal imaging conditions, smaller voxels could be used to achieve maximum resolution) and the CT image was reconstructed with 0.06 mm voxels. The CT image was reconstructed using the Feldkamp–Davis–Kress (FDK)[23] reconstruction framework which is a filtered-back projection algorithm for cone beam CT. SPECT images were reconstructed using a pixel-based ordered subset expectation maximization (POSEM)[24] algorithm and a calibration factor was applied to convert the SPECT measurements to concentrations (in MBq/mL). In all cases, a Gaussian smoothing window, ranging in size from 1.8 to 4 mm for the full width at half the maximum (fwhm) peak value, and decay correction based on the 6 h half-life of ^{99m}Tc were applied to the images prior to analysis. Figures showing the SPECT reconstructions in this paper show activities normalized to the calculated activity of the working solution for each data set for the starting time of the scans, therefore unitless, and presented in a color scale changing from blue (0) to red (1).

DOI: 10.1021/acs.est.6b04172
Environ. Sci. Technol. 2017, 51, 2864–2870

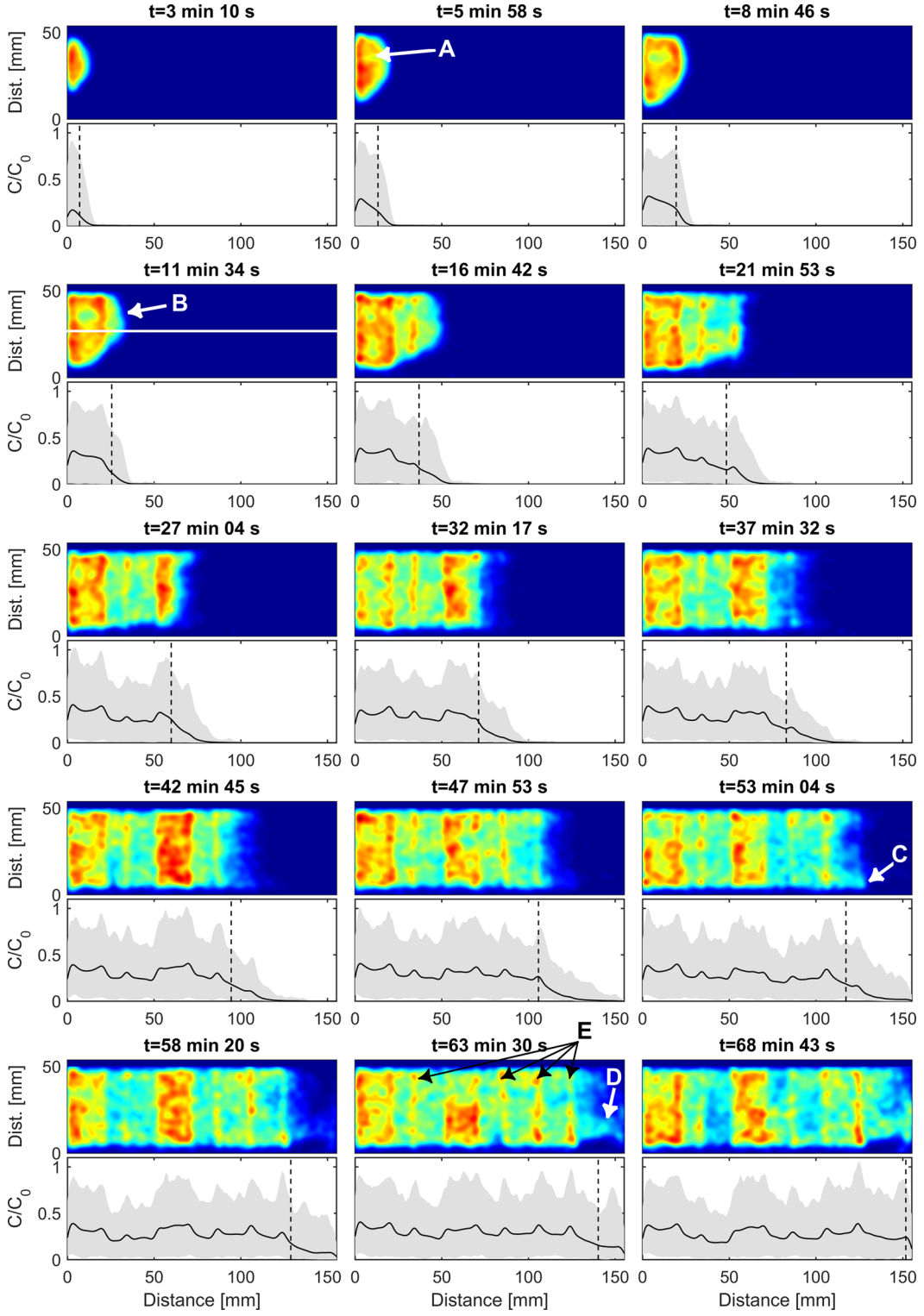

Figure 2. Horizontal cross sections extracted from the centers of time-lapse SPECT images of the ^{99m}Tc injection showing local (A) and global (B–D) nonuniform flow phenomena. Retention of ^{99m}Tc also occurs in the silica gel as well as in the soil and filter papers (E). These images share the same color scale with SPECT data presented in Figure 1 from 0 (blue) to 1 (red). Plots below each cross section show the slice averaged activity along the column for each time step (black line) and the range of the activities recorded throughout the column for that time step. The vertical dashed line in these plots indicates the mean travel distance of the plume calculated from the applied flux and assuming an average porosity of 40%.

RESULTS AND DISCUSSION

CT Imaging of Column Materials. A comparison between the photograph of the column and the CT scan is shown in Figure 1 images a and b. Individual grains are clearly visible in the CT image for the 0.5–4 mm glass beads (e.g., see inset image in Figure 1c). Individual grains of the 0.2 mm beads, silica gel, and soil are generally not identifiable, though soil texture and some larger soil grains/aggregates, pores, and cracks are visible. The capillary tubes are also clearly visible, with well-defined interior

DOI: 10.1021/acs.est.6b04172
Environ. Sci. Technol. 2017, 51, 2864–2870

and exterior edges for the 0.2 mm thick tube wall. These images therefore qualitatively suggest that in this experiment the CT scan can reliably resolve objects on the order of 200 μm and larger given the density contrast between the materials in the column.

High-Resolution Imaging with Long-Time (24 h) SPECT Observations. The SPECT images presented in Figure 1f–i are from a reconstruction of the first 24 h of data collected during the decay phase of the experiment and normalized to the calculated activity of the working solution (1.57 MBq/mL) at the beginning of decay scans. We present this particular image here as it represents the reconstruction with the best SPECT resolution obtained in this study. Furthermore, it was expected that the distribution of ^{99m}Tc should be relatively homogeneous within the pore space at this point in the experiment given that approximately two pore volumes of the spiked solution had been injected into the column. Figures 1f–h show enlarged views of the image extracted from the center of the column (parallel to the flow direction) given in Figure 1i. Rather than being homogeneously distributed, these images suggest that the ^{99m}Tc activity varies considerably (average 0.12 MBq/mL, ranging from 0 to 4.73 MBq/mL) both locally and macroscopically throughout the column. The SPECT images make it possible to locally compare the variability in the distribution of ^{99m}Tc to structural features observable in the CT scans.

Of the granular materials packed in the column, Figure 1i indicates that the highest activity (4.29 MBq in a 1 cm thick slice) is located in the soil layer (total activity calculated over 1 cm thick slices in other layers range from 2.5 MBq (silica gel) to 4.1 MBq (1 mm glass beads)). Unexpectedly, the glass-fiber filter papers between the layers also retained a substantial amount (average 0.43 MBq per 1 mm slice) of technetium (feature 1 in Figure 1). It is unclear why the soil and filter papers retained more technetium than other materials. One possible explanation could be related to increased porosity of these materials (~40% soil porosity) relative to the glass beads (ranging from 27% to 33% for 1–4 mm glass bead layers), thus a greater volume of pore space is available to hold more of the spike solution in these regions. Alternatively, it is also possible that the soil retained more technetium due to enhanced sorption resulting from higher surface area or more geochemically active surfaces than the glass beads. Although we have noticed trends between the porosity and total activity of the layers measured by the SPECT, we have not been able to fully discriminate between these two hypotheses with the available data.

Variability in ^{99m}Tc activity at the local scale is also significant. For the 4 mm glass beads (Figure 1h), low activity zones (mean value in the white circle (Figure 1h) is 0.07) in the SPECT data are consistent with the locations of individual beads in the CT scans (feature 2). Thus, the high-activity zones (average value for the feature 1 is 0.38) delineate pores where ^{99m}Tc is present. As the grain size decreases, distinct zones of high and low ^{99m}Tc continue to be present, but it is increasingly difficult to distinguish grains from pores. For the 2 mm size beads, for example, regions of high and low activity (ranging from 0.43 to 0.05) are still apparent, but there is substantial spatial blurring that causes activity to appear in regions where only grains should be present (feature 3). In areas where large pores are clearly present in the CT scan (feature 4), there is also a zone of high activity (on the order of 0.33–0.48) in the SPECT data. When the grain size is below the SPECT resolution, for example, for the 0.5 mm beads or soil, variations are still present in the ^{99m}Tc activity though no significant structural heterogeneities can be clearly identified in the CT scan at the same location for regions with either low activity (feature 6; 0 to 0.1) or high activity (feature 5; 0.2 to 0.4). It is not possible to clearly distinguish whether this variability is due to intrinsic limitations and artifacts of the imaging or localized variability of flow paths related to incomplete mixing along preferential flow paths within the material.

The influence of macropores on the ^{99m}Tc migration can be investigated by examining the activity distribution in the regions around the embedded capillary tubes. High activity levels (0.3 to 0.5), for example, are present around the capillary tube embedded in the 4 mm beads (i.e., Figure 1, feature 7). The linear zone of high activity observed near feature 7 indicates that high quantities of ^{99m}Tc are present in this area, but the resolution of the SPECT is insufficient to clearly determine whether this activity occurs within the 1.1 mm (inner) diameter of the capillary tube itself or in the surrounding region around the capillary tube. In contrast, a clear increase in activity is not observed near the capillary tube embedded in the 1 mm beads (feature 8, remains near background value of 0.2). The lack of activity here is apparently due to a physical blockage of the tube by a glass bead as shown in Figure 1d (feature 8). It is also apparent in the CT scan that the capillary tube disturbed the packing of the 4 mm grains creating a series of large connected pores, whereas the 1 mm beads packed more evenly and did not produce similar large pores. The macropores in the 4 mm beads would likely contain ^{99m}Tc and, therefore, be a probable source for the signal observed in this region in addition to ^{99m}Tc that might be held within the capillary tube itself.

Overall the CT data provide a useful reference for interpreting the SPECT image. The comparison between these imaging modalities qualitatively suggests that the practical resolution (e.g., smallest features with clear boundaries) of the SPECT images in this particular experiment are on the order of 1–2 mm. Even though the resolution of the SPECT images shown here may not typically allow for direct imaging of the distribution of ^{99m}Tc in individual pore spaces, the source of the observed activity can generally be associated with structural features when these features are large enough to be imaged by the CT scan. We therefore infer that variability in activity observed with the SPECT data is generally associated with flow and transport processes, suggesting that the SPECT may provide useful insights to the time evolution of these processes.

Time-Lapse Imaging of TcO_4^- Migration. Figure 2 shows 15 images obtained from the dynamic SPECT imaging during the period where the pump was turned on. The images presented here were normalized to the calculated activity of the working solution (3.06 MBq/mL) at the beginning of the scans and average bulk porosity of the column (40%) due to lower resolution nature of the data. These data are smoother with more blurred features than shown in Figure 1 as data for each image were collected over periods of only 2 to 3 min, resulting in a limited number of γ rays detected for use in image reconstruction compared to monitoring over a period of 24 h. These results show a complex, nonuniform evolution of ^{99m}Tc activity (average 0.25 MBq/mL, ranging from 0 to 1.55 MBq/mL) within the column over time. The overall activity range is not as wide as the high resolution SPECT image presented in Figure 1i. The persistence of low-activity regions within the ^{99m}Tc plume between different images through time suggests that these heterogeneities are related to nonuniform flow and transport phenomena in the column and not simply artifacts from random noise expressed in the image reconstruction.

DOI: 10.1021/acs.est.6b04172
Environ. Sci. Technol. 2017, 51, 2864–2870

The ^{99m}Tc initially entering the column on the left in Figure 2 spreads outward to fill the zone of silica gel. There is a notable asymmetry to the transport plume in the first 6 min of the experiment, however, as ^{99m}Tc appears to move around the location marked A. Low activities (around 0.5) generally persist in this region of the silica gel throughout the experiment. This behavior suggests the influence of a low-permeability zone that diverts flow around it.

Notably, the overall ^{99m}Tc radioactivity level in the silica gel is high (average 0.33) from the beginning of the experiment through the 68 min shown in Figure 2. This is in direct contrast to the situation shown in Figure 1, where the activity level in the silica gel is relatively low (average 0.1) compared to the rest of the column. The SPECT images collected during the flow portion of the experiment when the pump was stopped (not shown) are consistent with Figure 1 as they also have relatively low activity levels in the silica gel compared to the rest of the column. We have not yet been able to explain what could cause this discrepancy as the only differences in procedure were whether the pump was on or off and the length of time over which the data were acquired (i.e., 2 to 3 min for Figure 2 versus 10 min to 24 h for Figure 1). We do not expect that either of these differences in procedure should lead to the inconsistency in the silica gel activity observed.

Around 11 min into the experiment, the ^{99m}Tc begins to break through to the second zone, which contains the 0.2 mm glass beads. The ^{99m}Tc front in the upper part of the cross section appears to break through to this layer slightly faster than the bottom (feature B), thereby again creating an asymmetric plume. Throughout the experiment, the leading edge of the front continues to grow in the lower portion of the cross section as the top of the plume lags behind (feature C). Despite the fact that we did not intentionally include any large-scale heterogeneities in the column and do not observe any clear structural causes for this flow pattern in the CT scans, the ^{99m}Tc plume evolution suggests a macroscopic nonuniform flow behavior. As the ^{99m}Tc eventually reaches the far end of the column, there is evidence that the leading edge of the plume is transported along a flow path that channels upward toward the outlet in the center of the column (feature D).

The influences of the nonuniformity of flow are also expressed in breakthrough curves within the column (Figure 3). The breakthrough curves for five sample locations in a cross-sectional slice of the soil layer in the column (i.e., located at 60 mm from the inlet), the range of breakthrough curves for all voxels in the slice (shaded region), and the mean breakthrough curve for all voxels are shown in Figure 3a. While the mean transport across this slice yields a breakthrough curve typical of what we might expect in a standard outflow experiment, the gray zone in the figure shows that the variability of breakthrough behavior across this cross-section is substantial. Not only is there an apparent difference in the arrival times of the ^{99m}Tc at each voxel, but the magnitude of the normalized activities observed throughout the cross-section are also highly nonuniform, that is, ranging in the maximum relative activity from less than 0.4 to 0.8. The range of initial breakthrough times at each of these voxels varies from about 17−22 min, that is, a variation of about 25%, and maximum relative concentrations range from about 0.5 to almost 1. Notably, the breakthrough behavior of the ^{99m}Tc at these same locations further down the column (i.e., located at 115 mm from the inlet) shown in Figure 3b are a little more uniform with initial breakthrough time ranging around 37−40 min and maximum relative activity ranging from 0.4 to 0.6. The implication is that

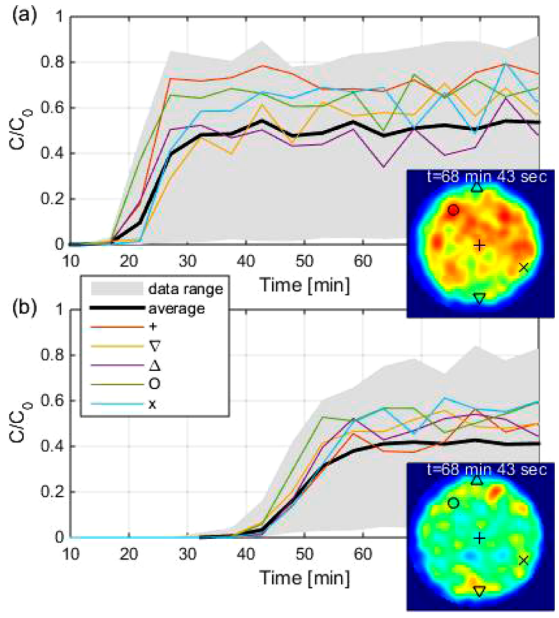

Figure 3. Range of the breakthrough curves showing the arrival of ^{99m}Tc for all the voxels (gray shaded area) with slice-averaged curves averaged over cross sections of different materials (black lines) and at individual voxels across the diameter of the column where the locations are marked on the cross section.

SPECT data, such as that shown here, can reveal information about heterogeneity in flow paths within a sample that we would normally expect to be homogeneous. In some scenarios, such preferential transport could cause a solute to experience substantially different geochemical conditions over time in a way that results in a different behavior than might otherwise be expected in a truly homogeneous material. This result indicates that additional work is needed to analyze SPECT images which can improve the value of the data for quantifying flow and transport processes.

Environmental Relevance. The examples described above illustrate how the 4D SPECT data inform both local and global flow processes. Despite the fact that the column was packed in relatively homogeneous layers, substantial nonuniformity in transport is observed. We would therefore expect that 4D SPECT imaging of a ^{99m}Tc tracer in materials with strong heterogeneities (e.g., fractures, macropores, or strong permeability contrasts) would allow for nonuniform flow paths to be mapped out, thus enabling us to better understand what portions of a porous medium with which a contaminant might have the opportunity to interact. Furthermore, the increased activity of ^{99m}Tc in the silica gel and soil, as well as the filter papers (feature E), points to the value of 4D SPECT for monitoring nonuniform accumulations of a tracer within a porous medium, which may have implications for understanding either physical or biogeochemical processes in a rock or soil. ^{99m}Tc was selected as a tracer for monitoring flow in porous media in this study not only because it can be imaged using SPECT but also because radionuclides such as ^{99}Tc and ^{129}I are also contaminants of concern at many DOE sites. Therefore, future SPECT imaging studies designed to understand fundamental biogeochemical processes in porous media using isotopes such as ^{125}I, ^{131}I, and ^{99m}Tc hold promise for understanding the larger-scale field behavior of these risk drivers.

DOI: 10.1021/acs.est.6b04172
Environ. Sci. Technol. 2017, 51, 2864−2870

■ ASSOCIATED CONTENT

Supporting Information

The Supporting Information is available free of charge on the ACS Publications website at DOI: 10.1021/acs.est.6b04172.

Chemical and physical characteristics of the SRS soil (PDF)

Timeline for the images collected during the experiment (PDF)

■ AUTHOR INFORMATION

Corresponding Author

*Phone: 864-656-2239; fax: 864-656-1041; e-mail: mdogand@clemson.edu. Address: Clemson University, Dept. of Environmental Engineering and Earth Sciences, L.G. Rich Environmental Laboratory, 342 Computer Court, Anderson, SC 29625.

ORCID

Mine Dogan: 0000-0001-7222-4490

Brian A. Powell: 0000-0003-0423-0180

Notes

The authors declare no competing financial interest.

■ ACKNOWLEDGMENTS

We thank the Associate Editor Daniel Giammar and four anonymous reviewers for their helpful comments in reviewing this manuscript. This material is based upon work supported by the U.S. Department of Energy Office of Science, Office of Basic Energy Sciences, and Office of Biological and Environmental Research under Award Number DE-SC-0012539.

■ REFERENCES

(1) Crestana, S.; Vaz, C. M. P. Non-invasive instrumentation opportunities for characterizing soil porous systems. *Soil Tillage Res.* **1998**, *47*, 19−26.

(2) Werth, C. J.; Zhang, C.; Brusseau, M. L.; Oostrom, M.; Baumann, T. A review of non-invasive imaging methods and applications in contaminant hydrogeology research. *J. Contam. Hydrol.* **2010**, *113*, 1−24.

(3) Liu, Y.; Liu, C.; Kukkadapu, R. K.; McKinley, J. P.; Zachara, J.; Plymale, A. E.; Miller, M. D.; Varga, T.; Resch, C. T. ^{99}Tc(VII) retardation, reduction, and redox state scaling in naturally reduced sediments. *Environ. Sci. Technol.* **2015**, *49*, 13403−13412.

(4) Amin, M. H. G.; Chorley, R. J.; Richards, K. S.; Bache, B. W.; Hall, L. D.; Carpenter, T. A. Spatial and temporal mapping of water in soil by magnetic-resonance imaging. *Hydrol. Processes* **1993**, *7* (3), 279−286.

(5) Sammartino, S.; Michel, E.; Capowiez, Y. A novel method to visualize and characterize preferential flow in undisturbed soil cores by using multislice helical CT. *Vadose Zone J.* **2012**, *11* (1), No. 000304802500027.

(6) Koestel, J.; Larsbo, M. Imaging and quantification of preferential solute transport in soil macropores. *Water Resour. Res.* **2014**, *50*, 4357−4378.

(7) Wildenschild, D.; Sheppard, A. P. X-ray imaging and analysis techniques for quantifying pore-scale structure and processes in subsurface porous medium systems. *Adv. Water Resour.* **2013**, *51*, 217−246.

(8) Davit, Y.; Iltis, G.; Debenest, G.; Veran-Tissoires, S.; Wildenschild, D.; Gerino, M.; Quintard, M. Imaging biofilm in porous media using x-ray computed microtomography. *J. Microsc.* **2011**, *242* (1), 15−25.

(9) Hao, N.; Moysey, S. M. J.; Powell, B. A.; Ntarlagiannis, D. Evaluation of surface sorption processes using spectral induced polarization and a ^{22}Na tracer. *Environ. Sci. Technol.* **2015**, *49*, 9866−9873.

(10) Corkhill, C. L.; Bridge, J. W.; Chen, X. C.; Hillel, P.; Thornton, S. F.; Romero-Gonzalez, M. E.; Banwart, S. A.; Hyatt, N. C. Real-time gamma imaging of technetium transport through natural and engineered porous materials for radioactive waste disposal. *Environ. Sci. Technol.* **2013**, *47*, 13857−13864.

(11) McKeighen, R. E. A review of gamma camera technology for medical imaging. In *Nuclear Medicine, Ultrasonics, and Termography*; Nudelman, S., Patton, D. D., Eds.; Springer: Des Plaines, IA, 1980; pp 119−163.

(12) Lear, G.; McBeth, J. M.; Boothman, C.; Gunning, D. J.; Ellis, B. L.; Lawson, R. S.; Morris, K.; Burke, I. T.; Bryan, N. D.; Brown, A. P.; Livens, F. R.; Lloyd, J. R. Probing the biogeochemical behavior of technetium using a novel nuclear imaging approach. *Environ. Sci. Technol.* **2010**, *44*, 156−162.

(13) Vandehey, N. T.; O'Neil, J. P.; Slowey, A. J.; Boutchko, R.; Druhan, J. L.; Moses, W. W.; Nico, P. S. Monitoring Tc dynamics in a bioreduced sediment: An investigation with gamma camera imaging of ^{99m}Tc-pertechnetate and ^{99m}Tc-DTPA. *Environ. Sci. Technol.* **2012**, *46*, 12583−12590.

(14) Jones, D. W., Hogg, P., Seeram, E., Eds. *Practical SPECT/CT in Nuclear Medicine*; Springer: New York, 2013.

(15) Perret, J.; Prasher, S. O.; Kantzas, A.; Hamilton, K.; Langford, C. Preferential solute flow in intact soil columns measured by SPECT scanning. *Soil Sci. Soc. Am. J.* **2000**, *64*, 469−477.

(16) Boutchko, R.; Rayz, V. L.; Vandehey, N. T.; O'Neil, J. P.; Budinger, T. F.; Nico, P. S.; Druhan, J. L.; Saloner, D. A.; Gullberg, G. T.; Moses, W. W. Imaging and modeling of flow in porous media using clinical nuclear emission tomography systems and computational fluid dynamics. *J. Appl. Geophysics* **2012**, *76*, 74−81.

(17) Vandehey, N. T.; Boutchko, R.; Druhan, J. L.; O'Neil, J. P.; Nico, P. S.; Slowey, A. J.; Moses, W. W. Performance evaluation of SPECT imaging system for sediment column imaging. *IEEE Trans. Nucl. Sci.* **2013**, *60* (2), 763−767.

(18) Pini, R.; Vandehey, N. T.; Druhan, J.; O'Neil, J. P.; Benson, S. M. Quantifying solute spreading and mixing in reservoir rocks using 3-D PET imaging. *J. Fluid Mech.* **2016**, *796*, 558−587.

(19) Van Audenhaege, K.; Van Holen, R.; Vandenberghe, S.; Vanhove, C.; Metzler, S. D.; Moore, S. C. Review of SPECT collimator selection, optimization, and fabrication for clinical and preclinical imaging. *Med. Phys.* **2015**, *42*, 4796−4813.

(20) Deleye, S.; Van Holen, R.; Verhaeghe, J.; Vandenberghe, S.; Stroobants, S.; Staelens, S. Performance evaluation of small-animal multipinhole μSPECT scanners for mouse imaging. *Eur. J. Nucl. Med. Mol. Imaging* **2013**, *40* (5), 744−58.

(21) Ivashchenko, O.; van der Have, F.; Villena, J. L.; Groen, H. C.; Ramakers, R. M.; Weinans, H. H.; Beekman, F. J. Quarter-millimeter-resolution molecular mouse imaging with U-SPECT^{+}. *Mol. Imag.* **2014**, *13*, 1−8.

(22) Beals, D. M.; Hayes, D. W. Technetium-99, iodine-129 and tritium in the waters of the Savannah River Site. *Sci. Total Environ.* **1995**, *173*, 101−115.

(23) Feldkamp, L.; Davis, L.; Kress, J. Practical cone-beam algorithm. *J. Opt. Soc. Am. A* **1984**, *1*, 612−619.

(24) Branderhorst, W.; Vastenhouw, B.; Beekman, F. J. Pixel-based subsets for rapid multi-pinhole SPECT reconstruction. *Phys. Med. Biol.* **2010**, *55* (7), 2023.

DOI: 10.1021/acs.est.6b04172
Environ. Sci. Technol. 2017, 51, 2864−2870